Large Eddy Simulations of a Stratified Shear Layer

Hieu T. Pham
Mechanical and Aerospace Engineering,
University of California, San Diego,
La Jolla, CA 92092
e-mail: h8pham@ucsd.edu

Sutanu Sarkar
Fellow ASME
Mechanical and Aerospace Engineering,
University of California, San Diego,
La Jolla, CA 92092
e-mail: sarkar@ucsd.edu

The performance of the large eddy simulation (LES) approach in predicting the evolution of a shear layer in the presence of stratification is evaluated. The LES uses a dynamic procedure to compute subgrid model coefficients based on filtered velocity and density fields. Two simulations at different Reynolds numbers are simulated on the same computational grid. The fine LES simulated at a low Reynolds number produces excellent agreement with direct numerical simulations (DNS): the linear evolution of momentum thickness and bulk Richardson number followed by an asymptotic approach to constant values is correctly represented and the evolution of the integrated turbulent kinetic energy budget is well captured. The model coefficients computed from the velocity and the density fields are similar and have a value in range of $0.01 - 0.02$. The coarse LES simulated at a higher Reynolds number $Re = 50,000$ shows acceptable results in terms of the bulk characteristics of the shear layer, such as momentum thickness and bulk Richardson number. Analysis of the turbulent budgets shows that, while the subgrid stress is able to remove sufficient energy from the resolved velocity fields, the subgrid scalar flux and thereby the subgrid scalar dissipation are underestimated by the model. [DOI: 10.1115/1.4026416]

1 Introduction

Stratified turbulence plays a crucial role in numerous environmental applications because it dictates the rate at which the energy is transferred from large scales to the small scales, where the energy is ultimately dissipated by molecular viscosity. Stratified turbulence can be generated by many processes, and the parallel shear flow between two streams having different velocity and density is a condition typically observed in the ocean and the atmosphere. In favorable conditions, a stratified shear layer develops Kevin–Helmholtz (KH) shear instabilities and forms large-scale billows, which subsequently break down into turbulence and mix the streams. Although there is a large volume of experimental and numerical work on the physics of stratified turbulence, the present systematic LES investigation of the canonical stratified free-shear layer will be a useful addition. It provides an assessment of the LES approach to modeling of stratified shear flows.

Laboratory experiments and DNS of a stratified shear layer have been performed in several previous studies [1–5]. The highest Reynolds number of DNS studies of the stratified shear layer is on the order of 5000 [6,7]. Here, the Reynolds number is defined as the ratio of $\Delta U \delta_\omega / \nu$, where ΔU is the velocity difference across the shear layer, δ_ω is the half-thickness, and ν is molecular viscosity. For practical applications, it is necessary to simulate stratified shear layers at much higher Reynolds number and the use of LES shows great potential. In a DNS, the flow fields are resolved down to the diffusive scales so that all scales of turbulence are computed. In an LES, only the large eddies are resolved, leaving the small scales parameterized by subgrid fluxes so that the computational cost is significantly reduced. LES models of stratified turbulence have been tested and improved in applications such as turbulence generated by stratified homogeneous shear, turbulent flows in a stratified channel. Notably, LES has been extensively used in the exploration of stratified atmospheric boundary layer [8,9], and the use of LES in oceanic applications is increasing [10]. LES models of the canonical shear layer have also been evaluated [11] but without stratification. In the present study, we assess the ability of LES with a dynamic eddy viscosity/ diffusivity model to capture buoyancy effects on the evolution of a stratified shear layer.

A stably stratified shear layer shows a qualitatively different evolution with respect to the neutrally stratified case. In the neutral case, the thickness of the shear layer grows linearly at a constant rate in the self-similar stage [12,13]. However, due to buoyancy, a stratified shear layer exhibits a reduction in growth rate after the initial linear growth. At late time, the turbulence decays and the thickness of the shear layer approaches an asymptotic value. Similarly, the bulk Richardson number, which is a measure of shear instability and often used in parameterizing buoyancy effects in applications, also asymptotes to a constant value at late time. In the budget of turbulent kinetic energy (TKE), the reduced production of TKE and the additional buoyancy flux term cause the energy balance to vary at different times throughout the evolution of the shear layer [1,2,4,5,14,15]. These are important dynamical features, and the ability of LES models to capture these physics needs to be investigated.

In the following sections, LES results of a stratified shear layer at two different Reynolds numbers, 5000 and 50, 000, will be analyzed to evaluate model performance. Both simulations are performed on the *same* computational grid using the same dynamic subgrid model, as discussed in Sec. 2. In Sec. 3, the low Re simulation is compared with results from the DNS database of Ref. [7] at Re = 5000. The differences between the two LES simulations are contrasted in Sec. 4 to examine how the model performance changes as the separation between the filter scale and the dissipative scale increases. The discussion on the assessment of the LES model concludes in Sec. 5.

2 Model Formulation

2.1 A Stratified Shear Layer. Following the DNS of Ref. [7], we consider two parallel streams of different density flowing in opposite directions. The expressions for the streamwise velocity and the density of such flow are given by

$$\langle u^* \rangle \langle z^* \rangle = \frac{\Delta U^*}{2} \tanh\left(\frac{z^*}{0.5\delta_{\omega,0}^*}\right)$$

$$\langle \rho^* \rangle (z^*) = \rho_0^* + \frac{\Delta \rho^*}{2} \tanh\left(\frac{z^*}{0.5\delta_{\omega,0}^*}\right)$$

where ΔU^* and $\Delta \rho^*$ are the velocity and density differences, respectively. The thickness of the shear layer is δ_ω and computed
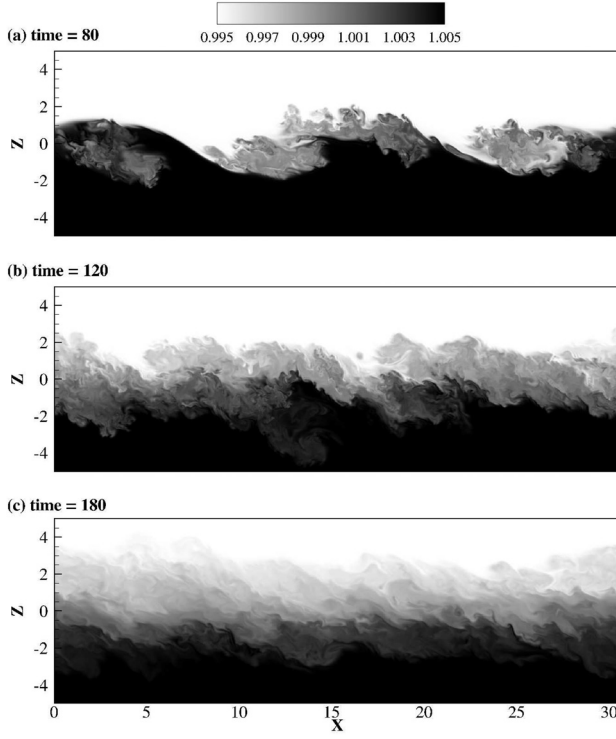
Fig. 1 Snapshots of the density field at various times in the DNS of a stratified shear layer [7]. Development of Kelvin–Helmholtz billows in (*a*) breakdown of the billows into turbulence in (*b*) and the late-time layer of decaying turbulence in (*c*) are important characteristics of a turbulent stratified shear layer.

Table 1 Nondimensional flow parameters and grid resolution used in the DNS of Ref. [7] and the present LES's. The resolution is normalized by the initial vorticity thickness $\delta_{\omega,0}$. The vertical grid spacing Δz is given in the region $-4.5 < z < 3$ for the DNS and in the region $-3 < z < 3$ for the LES. Outside this region, the spacing is increased at a rate of 1%.

Simulation	Re_0	$\mathrm{Ri}_{b,0}$	Pr	Δx	Δy	Δz	N_x	N_y	N_z
DNS	5000	0.1	1	0.03	0.03	0.03	1024	512	768
Fine LES	5000	0.1	1	0.12	0.12	0.03	256	128	512
Coarse LES	50,000	0.1	1	0.12	0.12	0.03	256	128	512

2.2 Governing Equations. In an LES, the equations of motion are filtered in space and take the following nondimensional form:

Mass.

$$\frac{\partial \overline{u_j}}{\partial x_j} = 0 \tag{1}$$

Momentum.

$$\frac{\partial \overline{u_i}}{\partial t} + \frac{\partial \left(\overline{u_j u_i} \right)}{\partial x_j} = -\frac{\partial \overline{P}}{\partial x_i} + \frac{1}{\mathrm{Re}_0} \frac{\partial^2 \overline{u_i}}{\partial x_j \partial x_j} - \mathrm{Ri}_{b,0} \overline{\rho'} g_i - \frac{\partial \tau_{ij}}{\partial x_j} \tag{2}$$

Density.

$$\frac{\partial \overline{\rho}}{\partial t} + \frac{\partial \left(\overline{u_j \rho} \right)}{\partial x_j} = \frac{1}{\mathrm{Re}_0 \mathrm{Pr}} \frac{\partial^2 \overline{\rho}}{\partial x_j \partial x_j} - \frac{\partial Q_j}{\partial x_j} \tag{3}$$

by $\Delta U^* / \max(|d\langle u^* \rangle / dz^*|)$. Here, we use the superscript $*$ to denote dimensional quantities, subscript 0 to denote initial quantities at time $t^* = 0$, and angle brackets $\langle \cdot \rangle$ to indicate quantities that are horizontally averaged in the streamwise (x) and spanwise (y) directions.

Figure 1 gives snapshots of the density field, showing three different stages of turbulence during the evolution of a stratified shear layer. During the first stage, the process of generation of fluctuations begins with KH shear instability at the center of the shear layer, where $z = 0$. The manifestation of the shear instability during the initial stage is wavelike, and correspondingly, the isopycnals inside the shear layer develop distinct troughs and crests with a characteristic wavelength. The instability subsequently develops into billows and braids shown in Fig. 1(*a*). The billows amalgamate with one another to create larger vortices, mostly through pairing but also tripling at some instances [5,15]. During the amalgamation, the fluid in the two streams is stirred and turbulence is seen inside the core of the billows as well as at the braids. The turbulence, generated by secondary shear instabilities and convective instability, is patchy and highly anisotropic at this stage, significantly different from homogeneous shear turbulence. In the second stage, the billows break down. At this time, as shown in Fig. 1(*b*), turbulence in the shear layer tends to homogenize the density, creating a central layer of mixed fluid that is approximately homogeneous in the horizontal. Turbulence at the edges of the shear layer actively entrains fluids from outside into the shear layer. The turbulent mixing rate at the edges is higher than inside the shear layer at this time. During the last stage, shown in Fig. 1(*c*), the turbulence decays, owing to stabilizing buoyancy effects until the shear layer becomes quiescent. Overall, the evolution of a stratified shear layer involves multiple turbulence generation processes that lead to turbulence with properties varying at different stages of the evolution, posing significant challenges for LES models.

where the overbar denotes filtered quantities and g denotes gravity acting in the vertical (z) direction. The subgrid stress τ_{ij} and subgrid buoyancy flux Q_j are to be parameterized by the LES model, as will be discussed in Sec. 2.3. The dimensionality in these equations has been normalized by ΔU^*, $\delta^*_{\omega,0}$, and $\Delta \rho^*$. The motion of the flow is prescribed by three nondimensional parameters: Reynolds number $\mathrm{Re}_0 = \Delta U^* \delta^*_{\omega,0} / \nu^*$, bulk Richardson number $\mathrm{Ri}_{b,0} = g^* \Delta \rho^* \delta^*_{\omega,0} / \rho^*_0 \Delta U^{*2}$, and Prandtl number $\mathrm{Pr} = \nu^* / \kappa^*$, where ν^* and κ^* are molecular viscosity and diffusivity, respectively. It is noted that quantities without the superscript $*$ are nondimensional. Two LES cases at Reynolds numbers 5000 and 50,000 are performed. The simulation with the smaller Re is for comparison with results from DNS of Ref. [7]. The larger Re simulation will determine the performance of LES when turbulence becomes more vigorous. The initial bulk Richardson and Prandtl numbers are kept the same in both simulations.

Parameters used in the present simulations are listed in Table 1. The Reynolds and bulk Richardson numbers used in the present study are relevant to the shear instabilities observed in equatorial undercurrents [6] as well as in near-field river plumes [16]. The observed Prandtl number is typically 7 for thermally stratified water and 700 for salt-stratified water. We use Prandtl of unity in the present study. In a previous DNS study, Ref. [6] shows that mixing efficiency can vary with Prandtl number. Nevertheless, in the present LES study, we focus on the performance of subgrid fluxes when the grid cutoff is larger than the Kolmogorov scale and, therefore, much larger than the Batchelor scale as Pr increases. The effect of high Pr is most significant during the early development of the KH billows, when density gradient can get sharper than velocity gradient due to smaller diffusivity. However, as the shear layer becomes turbulent, the subgrid viscosity and subgrid diffusivity is comparable (in the low-Re LES) and significantly larger (in the high-Re LES) than the molecular values. The use of unity Prandtl number, rather than higher values as in the

observation, would not change the LES results pertaining to turbulent processes in the present study.

2.3 Subgrid Models. There are many different types of LES models, e.g., the eddy viscosity model [17], the dynamic eddy viscosity model [18], and the similarity model [19]. Reference [11] performed simulations of a neutrally stratified mixing layer using different subgrid models, including the aforementioned three models, to show that the dynamic procedure at a low Reynolds number leads to better results than the constant eddy viscosity model, which is too dissipative during the growth of the billows and subsequent breakdown into turbulence. A mixed model that combines the dynamic eddy viscosity model and the similarity model produces the best performance. However, when simulated at a higher Reynolds number, the dynamic eddy viscosity model shows the best performance in capturing the self-similar turbulent statistics, and thus, it is adopted to compute the subgrid stress in the present study. The dynamic procedure has been used successfully in wall-bounded oceanic flows, e.g., a shallow channel with Langmuir turbulence [20]. An advantage of the dynamic procedure in the context of environmental flows is its ability to adapt to flow oscillation [21–23] encountered in tidal flows and flows with surface waves or internal gravity waves. A similar dynamic procedure is used to estimate the subgrid buoyancy flux within the framework of an eddy diffusivity model. The dynamic model for subgrid buoyancy flux has been successfully used to investigate stratified turbulence in wall-bounded flows, e.g., a channel [24,25], an Ekman bottom boundary layer [26], and a stratified oscillating bottom boundary layer [27].

The subgrid stress and subgrid buoyancy flux in an eddy viscosity model can be written as follows:

$$\tau_{ij} = -2C_d\overline{\Delta}^2|\overline{S}|\overline{S}_{ij} \tag{4}$$

$$Q_j = -C_\theta\overline{\Delta}^2|\overline{S}|\frac{\partial\overline{\rho}}{\partial x_j} \tag{5}$$

where $\overline{\Delta}$ is the filter width, $\overline{S}_{ij} = 1/2\left(\partial\overline{u}_i/\partial x_j + \partial\overline{u}_j/\partial x_i\right)$ is the resolved strain rate tensor, and $|\overline{S}|$ is defined as $\sqrt{2\overline{S}_{ij}\overline{S}_{ij}}$. The subgrid eddy viscosity and diffusivity are given by

$$\nu_{\text{sgs}} = C_d\overline{\Delta}^2|\overline{S}| \tag{6}$$

$$\kappa_{\text{sgs}} = C_\theta\overline{\Delta}^2|\overline{S}| \tag{7}$$

respectively. In a DNS, as in Ref. [7], the grid spacing needs to be sufficiently small to resolve scales as small as a few Kolmogorov length scales. In LES models, subgrid stresses and subgrid buoyancy flux provide the energy transfer to subfilter motion through the so-called subgrid dissipation so that grid spacing can be significantly coarser compared to DNS. In the fine LES at Re = 5000, we keep the vertical grid spacing at the same value as in Ref. [7]; however, the grid spacing in the horizontal directions is four times coarser. In the coarse LES, we increase Re to 50,000, effectively lowering the Kolmogorov length scale, while keeping the grid spacing as same as in the fine LES. It is of interest to see if the LES model can provide sufficient subgrid fluxes as the filter width becomes significantly larger than the Kolmogorov scale.

Following Refs. [18] and [28], the model coefficients C_d and C_θ are determined by a dynamic procedure in which a test filter is applied to the resolved velocity and density fields. Quantities denoted by $\widehat{\overline{\cdot}}$ are double-filtered with both the test and LES filters. The dynamic coefficient is given by

$$C_d = -\frac{1}{2}\frac{\langle L_{ij}M_{ij}\rangle}{\langle M_{ij}M_{ij}\rangle} \tag{8}$$

where

$$L_{ij} = \widehat{\overline{u}_i\overline{u}_j} - \widehat{\overline{u}}_i\widehat{\overline{u}}_j$$

$$M_{ij} = \widehat{\overline{\Delta}}^2\widehat{|\overline{S}|\overline{S}_{ij}} - \overline{\Delta}^2\widehat{|\overline{S}|\overline{S}_{ij}}$$

Similarly, the dynamic coefficient for the subgrid buoyancy flux is

$$C_\theta = -\frac{1}{2}\frac{\langle L_i^\theta M_i^\theta\rangle}{\langle M_j^\theta M_j^\theta\rangle} \tag{9}$$

where

$$L_i^\theta = \widehat{\overline{\rho}\overline{u}_i} - \widehat{\overline{\rho}}\widehat{\overline{u}}_i$$

$$M_i^\theta = \widehat{\overline{\Delta}}^2\widehat{|\overline{S}|\frac{\partial\overline{\rho}}{\partial x_i}} - \overline{\Delta}^2\widehat{|\overline{S}|\frac{\partial\overline{\rho}}{\partial x_i}}$$

The test filter is applied in physical space using an explicit three-point trapezoidal rule. The ratio of the test-to-LES filter width, $\widehat{\overline{\Delta}}/\overline{\Delta}$, is typically taken to be $\sqrt{6}$. The bracket $\langle.\rangle$ in Eqs. (8) and (9) denotes an average in the homogeneous directions (horizontal in the present problem). The averaging is used to smooth the large pointwise variation in the coefficients. When the coefficients are positive, implying that the model is purely dissipative, energy is transferred from the resolved to subgrid scales. In the rare event of the averaged C_d or C_θ being negative, the coefficients are clipped to zero to prevent numerical instability.

It is important to compare the magnitude of the filter size with the characteristic turbulent length scales to ensure that the cut-off filter width used in the model is sufficiently small to capture key dynamics of the flow. Figure 2 shows the evolution of the following scales at the center of the shear layer: Kolmogorov scale $\eta = (\nu^3/(\varepsilon + \varepsilon_{\text{sgs}}))^{1/4}$, Ozmidov scale $L_O = ((\varepsilon + \varepsilon_{\text{sgs}})/N^3)^{1/2}$, energy-containing scale $L_{EN} = K^{3/2}/(\varepsilon + \varepsilon_{\text{sgs}})$, and Ellison scale $L_E = (\rho')/d(\rho)/dz$. Here, K is turbulent kinetic energy and ε and ε_{sgs} are the resolved and subgrid dissipations, respectively. N^2 is the squared buoyancy frequency defined as $-g/\rho_0 d(\rho)/dz$. In Fig. 2, the length scales are normalized by the horizontal grid spacing Δx. The length scales shown in Fig. 2 are only relevant during the period of active turbulence, $50 < t < 200$. Over this period, all characteristic turbulent length scales are significantly larger than the cut-off grid spacing in both the fine and the coarse LES cases, except for the Kolmogorov scale. The Kolmogorov scale is reduced as Re gets larger, while the magnitudes of other length scales are qualitatively similar between the two LES cases. The energy-containing scale L_{EN}, visually seen to be the vertical size of the KH billows, is as large as 70 times the grid spacing. Interestingly, L_{EN} is an order of magnitude larger than both the Ozmidov scale (L_O) and the Ellison scale (L_E), showing that the largest scales at which stirring occurs in this flow are not limited by L_O or L_E. The Ozmidov and Ellison scales, scales at which buoyancy is important, are at least five times larger than the grid spacing when the flow becomes turbulent at $t = 80$. This confirms that the computational grid resolves the "large" eddies.

Another indicator of LES performance is the ability of the models to sufficiently remove energy at the grid scale. Figure 3 compares the energy spectra of the velocity fields E and density fields E_ρ between the DNS and the two LES's at time $t = 180$. All spectra show smooth decay at high wavenumber end, confirming sufficient removal of energy. The decay of the velocity spectrum in the fine (low-Re) LES in Fig. 3(a) matches well with the decay in the DNS spectrum. The velocity spectrum in the coarse (high-Re) LES shows higher energy at high wavenumber range; however, the rate of decay is comparable to that in the fine LES. The energy decay rate of the density spectra in the two LES's shown in Fig. 3(a) is also comparable to result of the DNS, although the energy is slightly lower at the tail end.
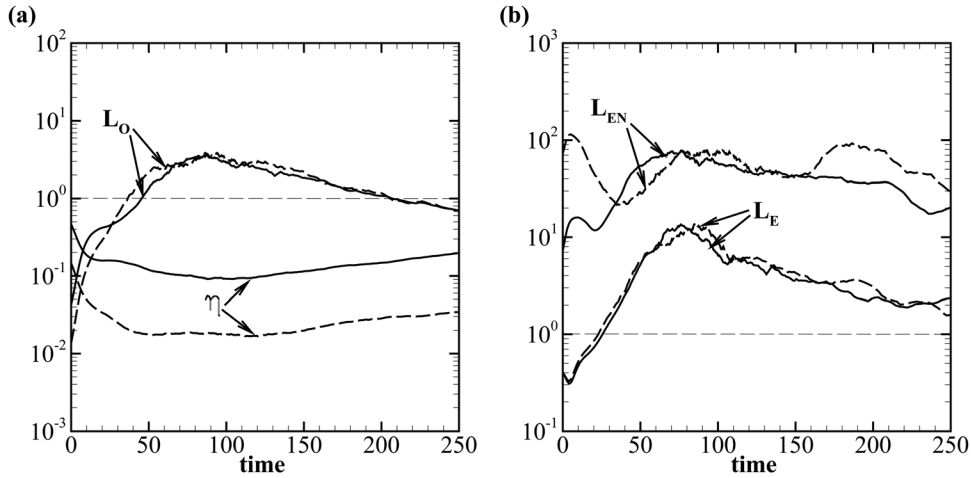
Fig. 2 Evolution of length scales at center of the shear layer in the LES models: (a) Kolmogorov scale η and Ozmidov scale L_O and (b) energy-containing scale L_{EN} and Ellison scale L_E. Solid lines and dash lines denote the fine (low-Re) and coarse (high-Re) LES models, respectively. The scales are normalized by the horizontal grid spacing $\Delta x = 0.12$.
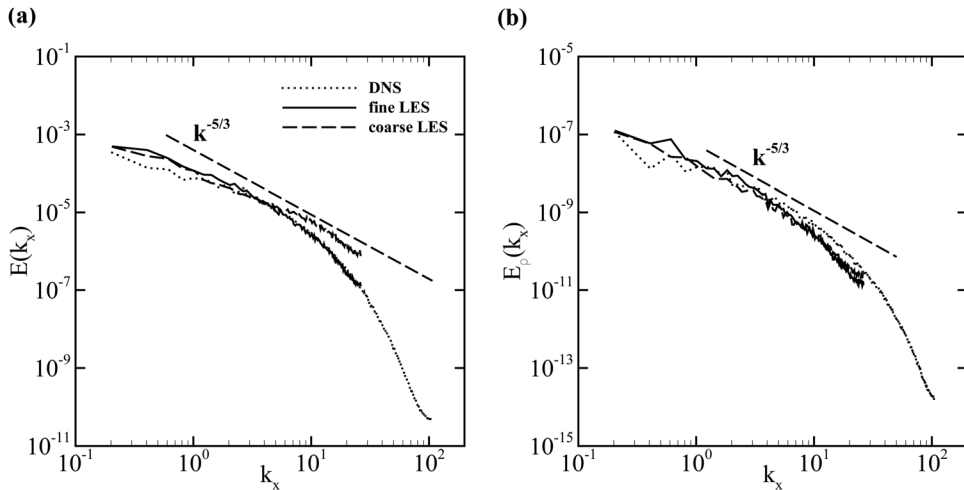
Fig. 3 Comparison of wavenumber spectra between the DNS and the LES cases at $t = 180$ and $z = 0$: (a) velocity fields and (b) density fields. The energy spectrum are plotted against the streamwise wavenumber k_x.

2.4 Numerical Methods. The computational domain for the LES is taken to be similar to Ref. [7] with $L_x = 30.75$, $L_y = 15.39$, and $L_z = 25.57$. The vertical grid spacing Δz in the LES is kept equal to that in the DNS so as to resolve the initial mean shear; however, the horizontal grid spacings (Δx and Δy) are four times coarser, reducing the number of grid points by a factor of 16. The numerical methods used in the present study are similar to those in Refs. [29] and [30]. A second-order central difference in space and a third-order Runge–Kutta marching in time are used to integrate Eqs. (2) and (3). A multigrid Poisson solver is used to compute the dynamic pressure. A sponge region is used in the regions $z < -10$ and $z > 10$ to damp any fluctuations propagating toward the upper and lower boundaries.

During the early evolution of the KH billows, sharp-density gradients are formed at the braids and the edges of the billows. In the LES models, due to the coarser grid, a density jump can occur over just one grid point, causing artificial oscillations on both sides of the jump. Since the flow dynamics in these regions is not turbulent, the LES model cannot provide subgrid fluxes that are sufficiently large to smooth out these oscillations. The oscillations can be removed by using alternative numerical methods designed specifically to capture sharp gradients, such as upwind schemes,

flux limiters, θ-method, etc. However, these methods have well-known drawbacks, such as high numerical dissipation. In the present study, we use explicit filtering to remove the numerical oscillations. A top hat filter is applied only to the density field at every 20 time steps and only at the nodes i that satisfy the following criteria:

$$\kappa_{sgs}/\kappa < 0.5$$
$$[\bar{\rho}(i+1) - \bar{\rho}(i)][\bar{\rho}(i) - \bar{\rho}(i-1)] < 0$$
$$[\bar{\rho}(i+1) - \bar{\bar{\rho}}(i)][\bar{\bar{\rho}}(i) - \bar{\rho}(i-1)] < 0$$

Here, i denotes the grid index, the double bars indicate the new filtered value of density, and the filtering is applied in all three directions. The first criterion limits the filtering operation to nonturbulent regions. The second criterion utilizes a sign change of first differences to limit the filtering to nodes where there are oscillations at grid scale. The last criterion ensures that the filtering does not create a new oscillation with opposite sign change of the first difference. It is noted that the operation does not damp out the background density gradient, since the gradient does not satisfy the last two limiting criterion. By using this filtering

scheme, we are able to remove the numerical oscillations while preserving the numerical method that we had used in the DNS. Explicit filtering has been used previously in the numerical simulations of Refs. [13] and [31].

In addition to the mean velocity and mean density profiles described above, small-amplitude zero-mean broadband velocity perturbations are also included in the initial conditions. The perturbations have the following energy spectrum:

$$E(k) = \left(\frac{k}{k_0}\right)^4 \exp\left[-2\left(\frac{k}{k_0}\right)^2\right]$$

where k is the horizontal wave number and k_0 is equal to 1.7. The amplitude of the perturbation is 1% ΔU. The horizontal boundaries have periodic conditions, while the top and bottom boundaries have the following conditions:

$$u(z_{\min}) = \frac{1}{2}, \quad u(z_{\max}) = \frac{-1}{2}$$
$$v(z_{\min}) = v(z_{\max}) = 0$$
$$\frac{\partial w}{\partial z}(z_{\min}) = \frac{\partial w}{\partial z}(z_{\max}) = 0$$
$$p(z_{\min}) = p(z_{\max}) = 0$$
$$\frac{\partial \rho}{\partial z}(z_{\min}) = \frac{\partial \rho}{\partial z}(z_{\max}) = 0$$

2.5 Budgets of Turbulence. In order to evaluate the performance of the LES models, it is important to characterize the roles of the subgrid fluxes in the TKE budget. The TKE budget for the simulated flow is described by the following equation:

$$\frac{dK}{dt} = P - \varepsilon + B - \frac{dT_3}{dz} - \varepsilon_{\text{sgs}} - \frac{dT_{3,sgs}}{dz} \tag{10}$$

where $K = 1/2\left\langle \bar{u}'_i \bar{u}'_j \right\rangle$ is the TKE. P is the production rate, defined as

$$P = -\langle \bar{u}' \bar{w}' \rangle \frac{d\langle \bar{u} \rangle}{dz}$$

ε is the dissipation rate, defined as

$$\varepsilon = \frac{2}{\text{Re}_0} \left\langle \bar{S}'_{ij} \bar{S}'_{ij} \right\rangle$$

and B is the buoyancy flux, defined as

$$B = -\text{Ri}_{b,0} \langle \bar{\rho}' \bar{w}' \rangle$$

The transport term dT_3/dz is defined with

$$T_3 = \frac{1}{2}\left\langle \bar{w}' \bar{u}'_i \bar{u}'_i \right\rangle + \frac{\langle \bar{p}' \bar{w}' \rangle}{\rho_0} - \frac{2}{\text{Re}_0}\left\langle \bar{u}'_i \bar{S}'_{3i} \right\rangle$$

The subgrid dissipation ε_{sgs} is defined as

$$\varepsilon_{\text{sgs}} = -\left\langle \tau'_{ij} \frac{\partial \bar{u}'_i}{\partial x_j} \right\rangle$$

The subgrid transport $dT_{3,\text{sgs}}/dz$ is defined with

$$T_{3,\text{sgs}} = \left\langle \tau'_{i3} \bar{u}'_i \right\rangle$$

Similarly, the performance of the subgrid buoyancy flux in the models can be seen in the budget of the density variance $\left\langle \bar{\rho}'^2 \right\rangle$, which is computed as follows:

$$\frac{d}{dt}\left\langle \bar{\rho}'^2 \right\rangle = P_\rho - \chi_\rho - \frac{dT_\rho}{dz} - \chi_{\rho,\text{sgs}} - \frac{dT_{\rho,\text{sgs}}}{dz} \tag{11}$$

where the scalar production P_ρ is defined as

$$P_\rho = -2\langle \bar{\rho}' \bar{w}' \rangle \frac{d\langle \bar{\rho} \rangle}{dz}$$

and the scalar dissipation χ_ρ is defined as

$$\chi_\rho = \frac{2}{\text{PrRe}_0}\left\langle \left(\frac{\partial \bar{\rho}'}{\partial x_i}\right)^2 \right\rangle$$

The transport term is

$$T_\rho = \left\langle \bar{\rho}'^2 \bar{w}' \right\rangle - \frac{1}{\text{PrRe}_0}\frac{\partial \left\langle \bar{\rho}'^2 \right\rangle}{\partial z}$$

The subgrid scalar dissipation $\chi_{\rho,\text{sgs}}$ is defined as

$$\chi_{\rho,\text{sgs}} = -2\left\langle Q'_i \frac{\partial \bar{\rho}'}{\partial x_i} \right\rangle$$

The subgrid transport term is defined as

$$T_{\rho,\text{sgs}} = \left\langle Q'_3 \bar{\rho}' \right\rangle$$

3 LES Performance at Low Reynolds Number

It is typical to compare results of LES models against results from filtered DNS, as in Ref. [11], because Eqs. (1)–(3) are solved for filtered quantities. However, we will present comparison with unfiltered DNS in the following discussion to examine whether the LES models can capture features observed in the DNS. Such comparison would be stringent because even a "perfect" LES is not expected to match with unfiltered DNS results. It is noted that filtering the DNS only changes small-scale dynamics, such as dissipation rate, but would not alter large-scale dynamics, such as mean quantities and the evolution of shear-layer thickness or bulk Richardson number.

3.1 Flow Evolution. Snapshots of the density fields, shown in Fig. 4, indicate that the fine (low-Re) LES is able to capture important dynamical features during the evolution of the stratified shear layer. At time $t = 80$, the primary mode of KH shear instability is similar between the DNS and the fine LES. Comparing Fig. 1(a) to Fig. 4(a), both simulations show a shear instability having similar horizontal wavelength and similar vertical extent of the KH billows. The secondary pairing of the billows seen in the DNS is also present in the fine LES at $x = 20$ in Fig. 4(a). In the DNS, there is an event where three vortices merge into a larger vortex; however, this is not seen in the LES. Without the triple pairing, the generation of turbulence in the fine LES is somewhat weaker than in the DNS at that time. When the KH billows break down into turbulence in the center region of the shear layer at $t = 120$, patches of localized turbulence are seen at the edges of the shear layer. The patches, caused by vortices that extend away from the center of the shear layer, can be seen in the DNS at $x = 13$ along the lower edge of the shear layer in Fig. 1(b). The fine LES also shows these patches along both the lower and upper edges, as in Fig. 4(b). At a later time $t = 180$, both Figs. 1(c) and 4(c) show the decay of turbulence in the shear layer. Unlike an unstratified shear layer, in which the turbulence approaches a self-similar state, the turbulence in a stratified shear layer is attenuated by buoyancy at late time. Such attenuation is an important feature that the fine LES is able to capture.
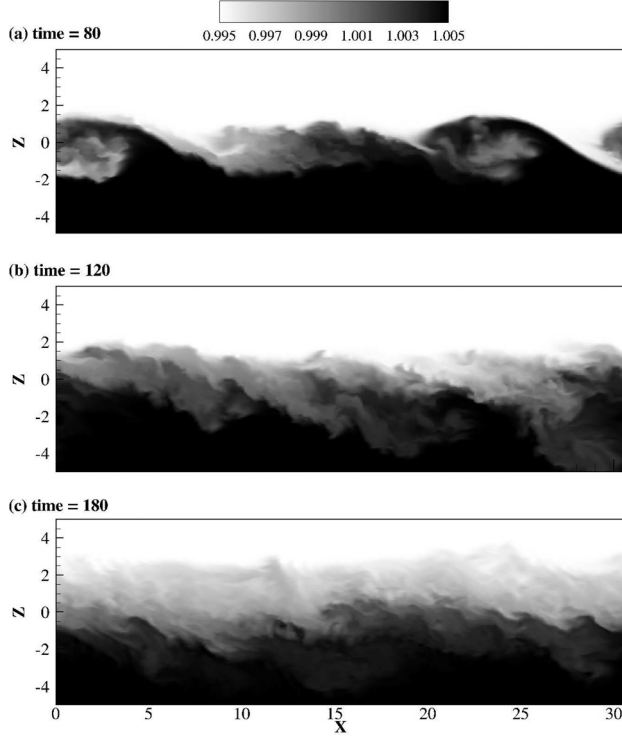
Fig. 4 Snapshots of the density field at various times in the fine (low-Re) LES. Similar to results of DNS, the LES captures the Kelvin–Helmholtz billows, their breakdown into turbulence, and the decay of turbulence.

We evaluate the growth of the shear layer by quantifying the temporal evolution of the momentum thickness, which is defined as follows:

$$\delta_\theta(t) = \int_{z_l}^{z_u} \left[\frac{1}{4} - \langle \bar{u}(t) \rangle^2 \right] dz$$

where z_u and z_l are the upper and lower boundary of the computational domain, excluding the sponge. Since δ_θ is an integral quantity, it can be used to assess if the LES can capture the overall evolution of the mean velocity $\langle u \rangle$. Figure 5(a) shows that the evolution of δ_θ is similar between the DNS and the fine LES. The evolution consists of a period of linear growth between $t = 50$ and 80, during which stage the KH billows form and amalgamate,

and a subsequent period of turbulent entrainment between $t = 80$ and $t = 200$. The thickness saturates after $t = 180$ at approximately four times its initial value. Relative to the DNS, the fine LES shows a smaller value of δ_θ during the initial growth period $70 < t < 100$ and a larger value during the turbulent entrainment period $t > 100$. The smaller value in the LES during the early period is due to the missing of the triple pairing, as discussed earlier. The larger value of δ_θ during the subsequent growth period suggests an overestimate in turbulent entrainment in the fine LES. Similar to δ_θ, the bulk Richardson number Ri_b also saturates after the turbulent entrainment period, as shown in Fig. 5(b). Both the DNS and LES indicate the same value at the end of the simulations, although the value fluctuates during the turbulent entrainment period. It is noted that Ri_b is computed using the vorticity thickness δ_ω, which, unlike the momentum thickness δ_θ, highly fluctuates in time. By definition, Ri_b represents the bulk ratio of potential energy to available mean kinetic energy, and its saturation implies that the mean kinetic energy can no longer be extracted for mixing. The ability to capture the evolution of Ri_b suggests the fine LES has correctly represented the bulk turbulent mixing of momentum and density.

3.2 Budgets of Turbulence. While the bulk characteristics of the shear layer are similar between the DNS and the fine (low-Re) LES, the turbulent statistics exhibit some differences. Figures 6(a) and 6(b) contrast the temporal evolution of the integrated TKE budgets between the DNS and the fine LES, respectively. In the figure, the terms in the TKE budget are integrated over the computational domain so that the resolved and subgrid transport terms are zero and *not* plotted. The evolution shows generation of TKE due to production at early time and decay of turbulence at later time due to dissipation and buoyancy flux. Between the two simulations, the DNS has a larger peak in the production, because the billows can amalgamate into larger vortices in this case. The larger vortices in the DNS result in a larger Reynolds stress than in the fine LES. Similarly, the dissipation rate in the DNS is also larger than the sum of resolved and subgrid dissipation in the LES. For example, at $t = 100$, the integrated dissipation in the DNS is 30% larger than the sum in the LES. It is noted that the dissipation rate computed from the filtered DNS, against which the LES should be compared, would be smaller than the values shown in Fig. 6(a). The smaller production also can contribute to the smaller dissipation seen in the LES. Different from the production and dissipation, the peaks in buoyancy flux, although occurring at different times, have a similar magnitude between the two simulations.

In an LES model, the energy at large scales is resolved while the energy at subfilter scales is removed by subgrid dissipation.
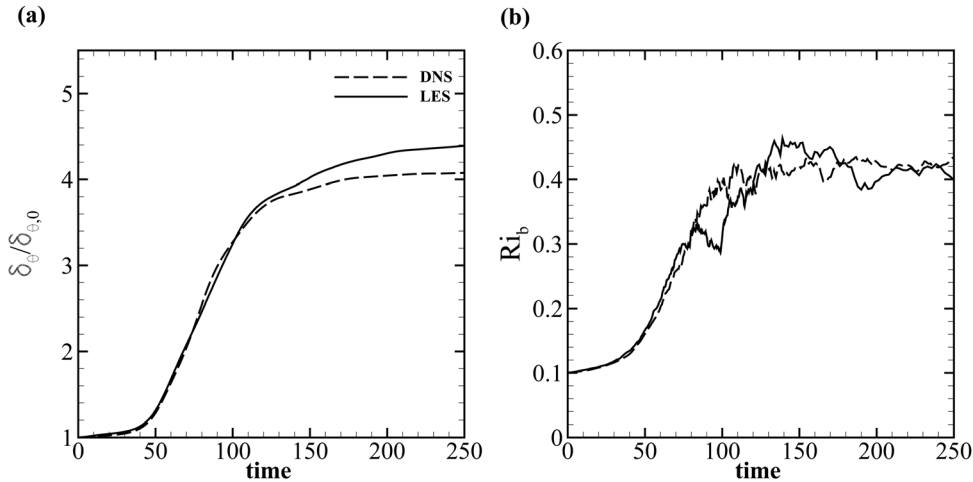
Fig. 5 Temporal evolution of (a) the momentum thickness δ_θ and (b) the bulk Richardson number Ri_b is similar between the DNS and the fine (low-Re) LES
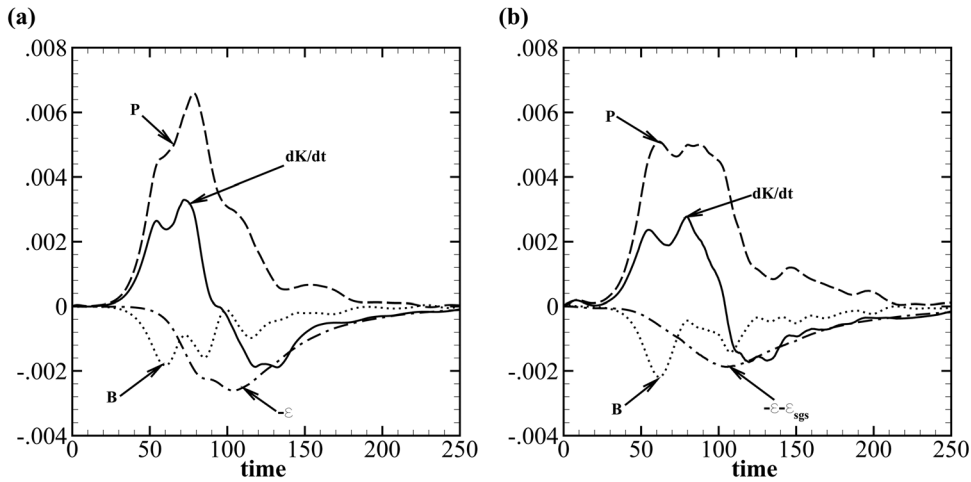
Fig. 6 Comparison of integrated turbulent kinetic energy budget over the computational domain in (*a*) the DNS and (*b*) the fine (low-Re) LES
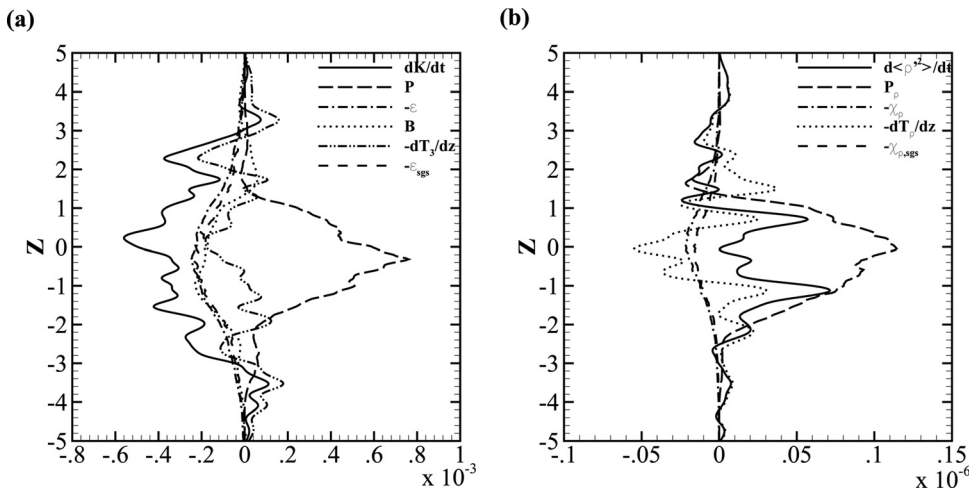

Fig. 7 Budgets of (*a*) the turbulent kinetic energy and (*b*) the density variance $\langle \rho'^2 \rangle$ at $t = 120$ in the fine (low-Re) LES

The capability of an LES to provide sufficient subgrid dissipation in the TKE budget is an important indicator of LES performance. The TKE budget at time $t = 120$ in the fine (low-Re) LES is shown in Fig. 7(*a*), and it indicates that the subgrid dissipation is a large contributor to the budget. At this time, although the production continues to generate turbulence, the TKE in the shear layer depletes due to a net loss. The decay of turbulence is caused by the loss to the buoyancy flux, the resolved dissipation, and the subgrid dissipation. The magnitudes of the transport, the buoyancy flux, and the resolved and subgrid dissipations are approximately equal to one another, and their sum is larger than the turbulent production at $z = 0$. While the subgrid dissipation is comparable to the resolved dissipation in the TKE budget, a different trend is seen in the budget of the density variance. Shown in Fig. 7(*b*), the subgrid scalar dissipation is noticeably smaller than the resolved scalar dissipation. At the center of the shear layer, the subgrid scalar dissipation is only 75% of the resolved contribution.

3.3 Behavior of Model Coefficients. The subgrid coefficient C_d from the fine (low-Re) LES has a range of values between 0.01 and 0.02 in the center region of the shear layer, $-3 < z < 3$, as shown in Fig. 8(*a*). This range of C_d is typical of previous applications to unstratified shear flows. At the edges of the shear layer where turbulence is intermittent (but can be strong), the

coefficient increases to larger values up to 0.03. Relative to the center of the shear layer, the edges have weaker stratification, and therefore, local turbulence can be stronger at times. The advantage of using a dynamic model is that the coefficient is allowed to dynamically adjust to local flow conditions, e.g., it is not excessively dissipative during the early evolution of the KH instability wave or during transition to turbulence, as demonstrated previously in the LES of a plane jet [32]. However, as discussed below, the internal wave activity in the stratified background must be handled conservatively. The coefficients in the nonturbulent region far away from the shear layer are nonzero at time $t = 80$. The nonzero coefficients are due to the presence of internal gravity waves. The LES model detects the velocity fluctuations due to wave activity and produces a nonzero model coefficient. At later times $t = 120$ and $t = 180$, the coefficients in the nonturbulent region have negative values that are set to zero to prevent numerical instability.

Despite the spatial scatter in the value of C_d, the horizontally averaged eddy viscosity $\langle \nu_{sgs} \rangle$ is confined to the shear layer, as shown in Fig. 8(*b*). The profiles of $\langle \nu_{sgs} \rangle$ have a peak value near the center and decay toward the edges of the shear layer. It is important to note that the profiles are shaped by the modulus of the strain rate $|\bar{S}|$, which effectively damps the effect of nonzero C_d in regions away from the shear layer. At time $t = 120$, the eddy viscosity at the center of the shear layer is approximately half of the molecular viscosity. While the eddy viscosity is smaller, the
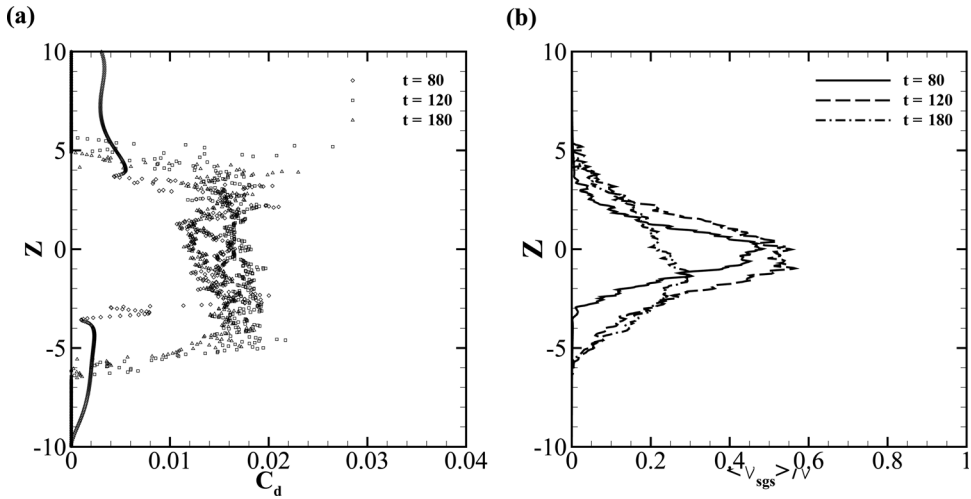
Fig. 8 (*a*) Dynamic subgrid coefficient C_d and (*b*) horizontally averaged eddy viscosity at various times in the fine (low-Re) LES
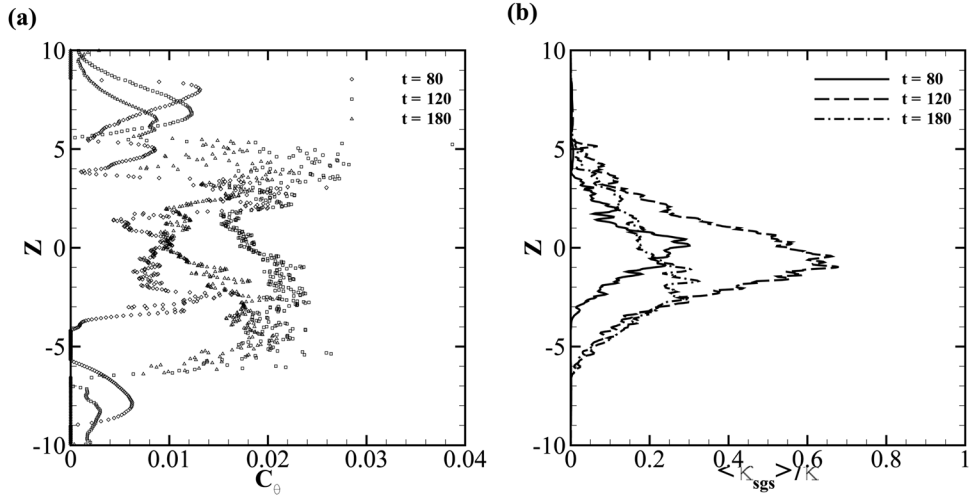
Fig. 9 (*a*) Dynamic subgrid coefficient C_θ and (*b*) horizontally averaged eddy diffusivity at various times in the fine (low-Re) LES

subgrid dissipation is as large as the resolved dissipation, as shown in Fig. 7(*a*). This is due to spatial variation in the eddy viscosity. Noting that, while ν is constant in space, ν_{sgs} varies spatially and proportionally with $|\bar{S}|$, the spatial distribution of eddy viscosity is skewed toward regions of large strain rate fluctuations, giving rise to a large subgrid dissipation.

Different from C_d which does not vary significantly, the model coefficient C_θ in the center shear layer fluctuates during the time period $80 < t < 180$. The coefficient has values notably smaller at early time $t = 80$ and at late time $t = 180$ compared to the value at time $t = 120$, as shown in Fig. 9(*a*). At $t = 120$, the coefficient has a range between $0.015 - 0.02$ in the center region of the shear layer. The coefficient also increases to larger values at the edges of the shear layer and have nonzero values in the regions far way, due to waves. While the spatial trend is similar between C_θ and C_d, the coefficients can have significant different values at the same depth, noting that the coefficients do not vary in horizontal planes. For example, at time $t = 80$, C_d at $z = 0$ is twice larger than C_θ. At time $t = 120$ and 180, negative values of C_d are clipped to zero in regions far away from the shear layer; however, C_θ has a positive value and, therefore, is not clipped.

The profiles of horizontally averaged eddy diffusivity $\langle \kappa_{sgs} \rangle$ are similar to those of $\langle \nu_{sgs} \rangle$: large values at the center decaying to

smaller values toward the edges of the shear layer, as shown in Fig. 9(*b*). The eddy diffusivity is considerably smaller than the molecular diffusivity. While the smaller $\langle \nu_{sgs} \rangle$ relative to ν gives comparable resolved and subgrid dissipation rates (ε and ε_{sgs} in Fig. 7(*a*)), the smaller $\langle \kappa_{sgs} \rangle$ relative to κ has the subgrid scalar dissipation smaller than the resolved part (χ and χ_{sgs} in Fig. 7(*b*)). The temporal evolution of the eddy diffusivity also varies differently from that of the eddy viscosity at the center of the shear layer. At this location, the subgrid Prandtl number, $Pr_{sgs} = \langle \nu_{sgs} \rangle / \langle \kappa_{sgs} \rangle$, has a value of 1.9, 0.9, and 1.3 at $t = 80$, 120, and 180, respectively.

4 LES Performance at High Reynolds Number

4.1 Flow Evolution. The coarse LES model simulated at a higher Reynolds number is also able to capture key dynamical features during the evolution of the stratified shear layer. Figure 10 shows snapshots of the density fields at three different stages of the evolution. The formation of KH billows in Fig. 10(*a*) and their breakdown to turbulence in Fig. 10(*b*) are similar to those in the fine LES discussed in Sec. 3.1. At late time, when turbulence decays, the shear layer is capped by the effects of stratification
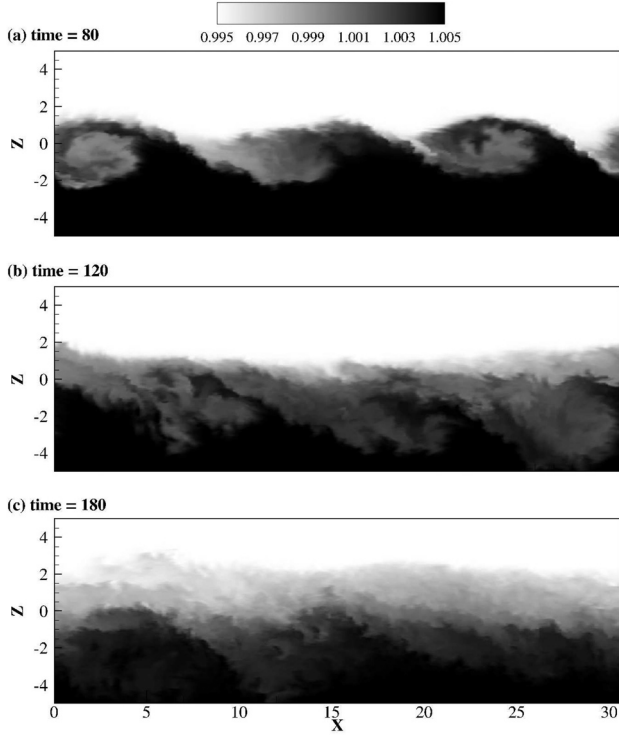
Fig. 10 Snapshots of the density field at various times in the coarse (high-Re) LES. The development of Kelvin–Helmholtz billows and the evolution of turbulence are well captured.

and becomes laminar, as in Fig. 10(c). Despite the difference in Re, the wavelength and the structure of the primary KH shear instability are similar between the two LES cases. However, we note the development of secondary instabilities, which only occur in the high-Re LES. In the fine (low-Re) LES, the braids connecting the billows maintain sharp density gradient until small-scale turbulence spreads from the billows and destroys the gradient. In the coarse (high-Re) LES, density overturns relating to secondary shear instabilities occur locally in the braids and generate turbulence there before the spread of turbulence from the billows, as seen in Fig. 10(a). The secondary instability occurred in the coarse LES has been seen previously in the observations. For example, Ref. [16] reports primary KH shear instabilities in the near field of a river plume exhibit secondary density overturns at the braids when the Reynolds number is large.

The bulk characteristics of the shear layer are also well captured. Figure 11(a) compares the temporal evolution of the momentum thickness δ_θ between the fine (low-Re) and coarse (high-Re) LES simulations. The initial growth rate during the development of the KH billows is similar. The period of linear growth ends at approximately $t = 100$ in the fine LES, while it extends a little longer in the coarse LES, resulting in a larger value of δ_θ. During the active turbulent period, $100 < t < 180$, δ_θ increases at a faster rate in the coarse LES. Due to larger turbulent entrainment at a higher Reynolds number, δ_θ grows to a larger value at the end of the simulation. At a higher Reynolds number, the shear layer can extract more momentum from the mean shear and grow to a larger thickness. This result is consistent with previous DNS study [4], which shows that the final Ri_b increases with increasing initial Re. Despite the difference in the final value, the coarse LES also captures the late-time buoyancy-induced saturation in the thickness. The evolution of the bulk Richardson number Ri_b in the coarse LES, shown in Fig. 11(b), is similar to that in the fine LES, except during the period $150 < t < 200$. In both cases, Ri_b saturates at the same value at late time.

4.2 Budgets of Turbulence. The TKE budget at time $t = 120$ in the coarse (high-Re) LES is shown in Fig. 12(a). The turbulent production reaches a slightly larger value at this time compared to the fine LES. Furthermore, the production integrated over the domain has a higher peak value in the coarse LES (not shown), indicating the shear layer in the high-Re simulation generates more TKE. Different from the fine LES, the subgrid dissipation is significantly larger than the resolved dissipation, although the total dissipation is approximately equal between the two LES simulations at this time. At the center of the shear layer, the subgrid dissipation is approximately ten times larger than the resolved value. With increasing Re, the subgrid stress contributes more to the TKE budget, making up for the smaller resolved dissipation. It is interesting to note that the dissipation rate provided by the LES model in the coarse (high-Re) simulation matches well with values reported in observations. The KH shear instability in the river plume reported in Ref. [16] with Re $\approx 5 \times 10^5$, $Ri_b \approx 0.2 - 0.25$, and Pr ≈ 700 has a dissipation rate in the core of the billows in range of $1 - 3 \times 10^{-4} (\mathrm{m^2 s^{-3}})$. Figure 12(a) shows the dissipation rate equal to $4.3 \times 10^{-4} (\mathrm{m^2 s^{-3}})$ at the center of the shear layer using $\Delta U = 1 \,\mathrm{ms^{-1}}$ and $\delta_\omega = 1 \,\mathrm{m}$, which are the scales observed in Ref. [16].

Similar to the TKE budget, the budget of density variance at time $t = 120$ shown in Fig. 12(b) also has the subgrid scalar dissipation significantly larger than the resolved contribution. While the ratio of the subgrid dissipation to the resolved dissipation in
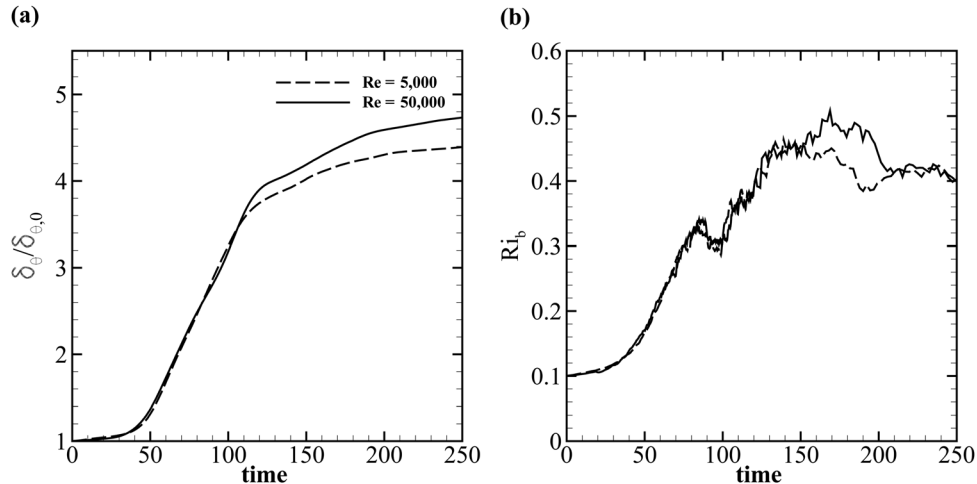
Fig. 11 Comparison of (a) the momentum thickness δ_θ and (b) the bulk Richardson number Ri_b between the fine (low-Re) and the coarse (high-Re) LES cases
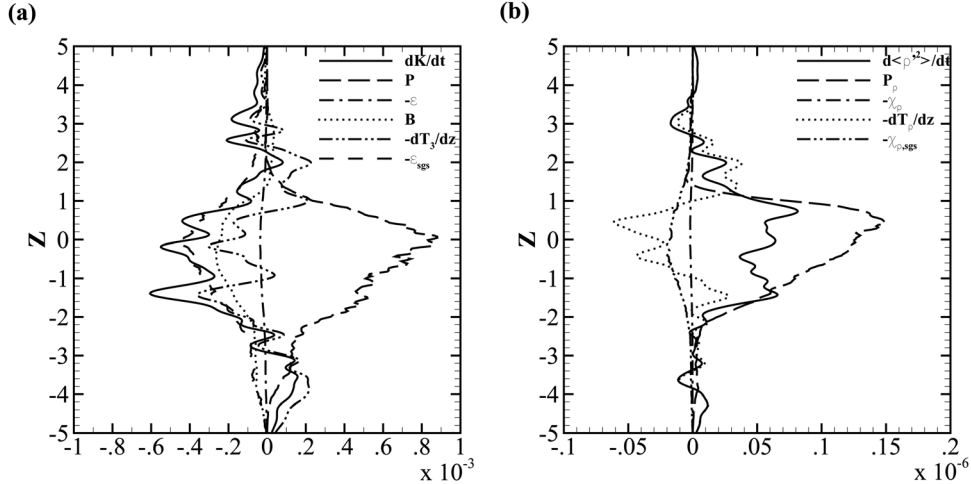
Fig. 12 Budgets of (*a*) the turbulent kinetic energy *K* and (*b*) the density variance $\langle \rho'^2 \rangle$ at $t = 120$ in the coarse (high-Re) LES
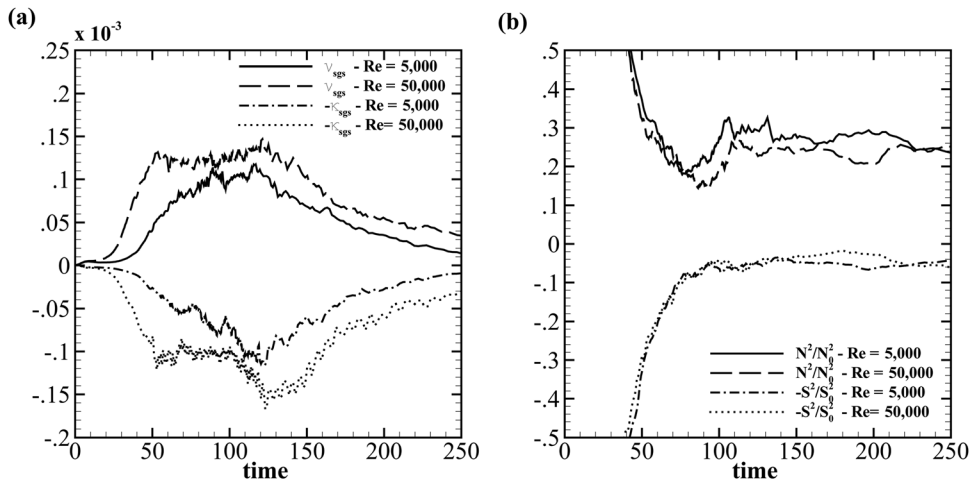
Fig. 13 (*a*) Difference in the eddy viscosity and eddy diffusivity at *z* = 0 between the fine (low-Re) and coarse (high-Re) LES cases and (*b*) evolution of squared shear rate S^2 and squared buoyancy frequency N^2 at the same location

the TKE budget in the coarse (high-Re) LES is 10:1, the ratio is only 7:1 in the budget of density variance. The difference suggests the subgrid stress and the subgrid scalar flux operate differently in the LES model. Furthermore, while the total dissipation of TKE is approximately equal between the two LES cases, the total scalar dissipation is smaller in the coarse simulation.

4.3 Behavior of Model Coefficients. The model coefficient C_d in the coarse (high-Re) LES has a range of values comparable to that in the fine (low-Re) LES. During the time period $80 < t < 180$, C_d falls in the range of $0.01 - 0.02$ in the central region and has a larger value, up to 0.3, at the edges of the shear layer. The model also produces nonzero values of C_d, as well as C_θ, due to effect of the internal gravity waves, in regions far away from the shear layer as in the fine LES. The value of C_d in the central region of the shear layer does not vary significantly between the two simulations. With a tenfold increase in Re, the value of C_d remains within the same range, suggesting that the subgrid viscosity depends mainly on the local strain rate $|S|$.

Figure 13(*a*) compares the horizontally averaged eddy viscosity and eddy diffusivity at $z = 0$ between the two LES cases. Overall,

the eddy viscosity is larger in the high-Re number simulation at all time. The larger eddy viscosity results in a larger subgrid dissipation in the TKE budget shown in Fig. 12(*a*). The difference between the two LES cases is largest during the development of the KH billows at time $t < 80$ when the shear layer is not yet fully turbulent. The shear rate, and consequently $|\bar{S}|$, is smaller in the fine LES during this period. The reason is that, in the fine LES at low Re, the larger molecular mixing of momentum causes $|\bar{S}|$ to decrease at a faster rate. A similar effect is seen in the eddy diffusivity during the same time period. During the period of decaying turbulence, $t > 120$, the difference in eddy diffusivity between the two LES cases is notably larger than the difference in eddy viscosity. However, the subgrid dissipation increases faster than the subgrid scalar dissipation when comparing Fig. 7 to Fig. 12.

Despite differences in the eddy viscosity and eddy diffusivity, the evolution of the mean quantities at the center of the shear layer, such as the squared shear rate S^2 and squared buoyancy frequency N^2, is similar between the two LES cases, as shown in Fig. 13(*b*). During the early stage, $0 < t < 80$, when the KH billows develop, both N^2 and S^2 are rapidly reduced. The billows reduce the momentum and the density differences between the two streams. During the decay stage, $t > 120$, S^2 and N^2 remain

relatively constant with the value in the coarse LES slightly smaller. The smaller N^2 and S^2 during this period are due to higher rate of mixing achieved at a higher Reynolds number. During the time period $80 < t < 120$, the center of the shear layer shows an increase in N^2, while S^2 remains relatively at the same value in both LES's. The increase in stratification in the center of the shear layer during this period is due to stronger mixing at the edges of the shear layer. During this period, turbulence at the edges actively entrains fluids of different density from the exterior into the shear layer so that the density difference across the center of shear layer gets larger, resulting in higher values of N^2.

5 Conclusions

In the present study, we have performed an assessment of the LES approach in the canonical case of a stratified shear layer. A dynamic procedure is used to compute model coefficients based on a test filter. The same dynamic procedure is applied to both the velocity field and the density field to yield two corresponding model coefficients, C_d and C_θ, which are used to compute the subgrid stress and the subgrid buoyancy flux, respectively. Two LES cases at different Reynolds numbers are performed on the same computational grid to evaluate the performance of the LES in high-Re applications.

The fine LES with Re = 5000, when compared with the DNS results at the same Re [7], shows excellent agreement. The evolution of the shear instability, including the growth of KH shear instability, the formation, pairing and breakdown of KH billows, and the decay of stratified turbulence, is well captured in the fine LES. The bulk characteristics of the shear layer, such as the temporal evolution of the momentum thickness, the bulk Richardson number, and the integrated TKE budget, agrees with the DNS results. In the TKE budget, at the times when the shear layer is turbulent, the subgrid dissipation has the same magnitude as the resolved dissipation. At the same time, the budget of the density variance shows that the subgrid scalar dissipation is significantly smaller than the resolved dissipation. The LES model yields the coefficients C_d and C_θ in the same range of $0.01 - 0.02$ in the shear layer. The horizontally averaged eddy viscosity and eddy diffusivity are smaller than the corresponding molecular values over the duration of the simulation.

The coarse LES at Re = 50, 000 also yields acceptable results in term of the bulk characteristics of the shear layer. The evolution of the KH shear instability and the generation of turbulence in the shear layer are captured in the model. The momentum thickness is approximately 10% larger than the value seen in the low-Re LES at late time, consistent with previous DNS study of the effect of initial Re [4]. The bulk Richardson number also asymptotes at late time at a value similar to that in the low-Re case. The TKE budget during the turbulent stage has subgrid dissipation significantly larger than the resolved dissipation, and the same trend is observed in the budget of the density variance. However, the ratio of the subgrid contribution to the resolved contribution is larger in the TKE budget, indicating the subgrid buoyancy flux does not increase as much as the subgrid stress as Reynolds number increases. At a higher Re, the subgrid dissipation increases as the horizontally averaged eddy viscosity increases. In contrast, while the eddy diffusivity also increases at higher Re, the subgrid scalar dissipation does not significantly increase. This suggests that, as Re increases, the density gradient at the grid scale does not align with the velocity gradient, which the LES model uses to compute eddy diffusivity.

Acknowledgment

References

[1] Smyth, W. D., and Moum, J. N., 2000, "Length Scales of Turbulence in Stably Stratified Mixing Layers," Phys. Fluids, **12**(6), pp. 1327–1342.
[2] Smyth, W. D., and Moum, J. N., 2000, "Anisotropy of Turbulence in Stably Stratified Mixing Layers," Phys. Fluids, **12**(6), pp. 1343–1362.
[3] Caulfield, C. P., and Peltier, W. R., 2000, "The Anatomy of the Mixing Transition in Homogeneous and Stratified Free Shear Layers," J. Fluid Mech., **413**, pp. 1–47.
[4] Brucker, K., and Sarkar, S., 2007, "Evolution of an Initially Turbulent Stratified Shear Layer," Phys. Fluids, **19**, p. 101105.
[5] Pham, H. T., Sarkar, S., and Brucker, K. A., 2009, "Dynamics of a Stratified Shear Layer Above a Region of Uniform Stratification," J. Fluid Mech., **630**, pp. 191–223.
[6] Smyth, W. D., Moum, J. N., and Caldwell, D. R., 2001, "The Efficiency of Mixing in Turbulent Patches: Inferences From Direct Simulations and Microstructure Observations," J. Phys. Oceanogr., **31**, pp. 1969–1992.
[7] Pham, H. T., and Sarkar, S., 2010, "Transport and Mixing of Density in a Continuously Stratified Shear Layer," J. Turbulence, **11**, pp. 1–23.
[8] Moeng, C., and Sullivan, P., 1994, "A Comparison of Shear- and Buoyancy-Driven Planetary Boundary Layer Flows," J. Atmos. Sci., **51**(7), pp. 999–1022.
[9] Chamecki, M., Meneveau, C., and Parlange, M., 2007, "The Local Structure of Atmospheric Turbulence and Its Effect on the Smagorinsky Model for Large Eddy Simulation," J. Atmos. Sci., **64**, pp. 1941–1958.
[10] Scotti, A., 2010, "Large Eddy Simulation in the Ocean," Intl. J. Comput. Fluid Dyn., **24**, pp. 393–406.
[11] Vreman, B., Geurts, B., and Kuerten, H., 1997, "Large-Eddy Simulation of the Turbulent Mixing Layer," J. Fluid Mech., **339**, pp. 357–390.
[12] Rogers, M. M., and Moser, R. D., 1994, "Direct Simulation of a Self-Similar Turbulent Mixing Layer," Phys. Fluids, **6**, pp. 903–923.
[13] Pantano, C., and Sarkar, S., 2002, "A Study of Compressibility Effects in the High-Speed Turbulent Shear Layer Using Direct Simulation," J. Fluid Mech., **451**, pp. 329–371.
[14] Thorpe, S. A., 1973, "Experiments on Instability and Turbulence in a Stratified Shear Flow," J. Fluid Mech., **61**, pp. 731–751.
[15] Koop, C. G., and Browand, F. K., 1979, "Instability and Turbulence in a Stratified Fluid With Shear," J. Fluid Mech., **93**, pp. 135–159.
[16] Geyer, W. R., Lavery, A. C., Scully, M. E., and Trowbridge, J. H., 2010, "Mixing by Shear Instability at Higher Reynolds Number," Geophys. Res. Lett., **37**(22), pp. 1–5.
[17] Smagorinsky, J., 1963, "General Circulation Experiments With the Primitive Equations I. The Basic Experiment," Mon. Weather Rev., **91**, pp. 99–164.
[18] Germano, M., Piomelli, U., Moin, P., and Cabot, W., 1991, "A Dynamic Subgrid-Scale Eddy Viscosity Model," Phys. Fluids, **3**, pp. 1760–1765.
[19] Bardina, J., Ferziger, J., and Reynolds, W., 1980, "Improved Subgrid Models for Large Eddy Simulation," AIAA Paper No. 80-1357.
[20] Tejada-Martinez, A. E., and Grosch, C. E., 2007, "Langmuir Turbulence in Shallow Water. Part 2. Large-Eddy Simulation," J. Fluid Mech., **576**, pp. 63–108.
[21] Scotti, A., and Piomelli, U., 2001, "Numerical Simulation of Pulsating Turbulent Channel Flow," Phys. Fluids, **13**, pp. 1367–1384.
[22] Salon, S., Armenio, V., and Crise, A., 2007, "A Numerical Investigation of the Stokes Boundary Layer in the Turbulent Regime," J. Fluid Mech., **570**, pp. 253–296.
[23] Radhakrishnan, S., and Piomelli, U., 2008, "Large-Eddy Simulation of Oscillating Boundary Layers: Model Comparison and Validation," J. Geophys. Res., **113**, p. C02022.
[24] Armenio, V., and Sarkar, S., 2002, "An Investigation of Stably-Stratified Turbulent Channel Flow Using Large Eddy Simulation," J. Fluid Mech., **459**, pp. 1–42.
[25] Taylor, J. R., Sarkar, S., and Armenio, V., 2005, "Large Eddy Simulation of Stably Stratified Open Channel Flow," Phys. Fluids, **17**(116602), pp. 1–18.
[26] Taylor, J. R., and Sarkar, S., 2007, "Internal Gravity Waves Generated by a Turbulent Bottom Ekman Layer," J. Fluid Mech., **590**, pp. 331–354.
[27] Gayen, B., Sarkar, S., and Taylor, J. R., 2010, "Large Eddy Simulation of a Stratified Boundary Layer Under an Oscillatory Current," J. Fluid Mech., **643**, pp. 233–266.
[28] Lilly, D. K., 1992, "A Proposed Modification of the Germano Subgrid-Scale Closure Method," Phys. Fluids A, **4**, pp. 633–635.
[29] Basak, S., and Sarkar, S., 2006, "Dynamics of a Stratified Shear Layer With Horizontal Shear," J. Fluid Mech., **568**, pp. 19–54.
[30] Brucker, K. A., and Sarkar, S., 2010, "A Comparative Study of Self-Propelled and Towed Wakes in a Stratified Fluid," J. Fluid Mech., **652**, pp. 373–404.
[31] Slinn, D. N., and Riley, J. J., 1998, "A Model for the Simulation of Turbulent Boundary Layers in an Incompressible Stratified Flow," J. Comput. Phys., **144**, pp. 550–602.
[32] Le Ribault, C., Sarkar, S., and Stanley, S. A., 1999, "Large Eddy Simulation of a Plane Jet," Phys. Fluids, **11**(10), pp. 3069–3083.